Investigation on structural and magnetic properties of the mechano-synthesized Fe-doped ZrO$_2$-15 mol% Y$_2$O$_3$

Ali Sari[1,2,*], Mourad Keddam[3], Abdelkader Ouanezar[1], Abderrahim Malki[1]

[1]*Nuclear Research Center of Birine, Box 180 Ain Oussera, Djelfa, Algeria*

[2]*Laboratory of Materials Technology, Faculty of Mechanical Engineering and Processing, USTHB, B.P. No. 32, 16111 El-Alia, Bab-Ezzouar, Algiers, Algeria*

[3]*Materials Technology Laboratory, Faculty of Mechanical Engineering and Chemical Processing, USTHB, B.P. No. 32, 16111 El-Alia, Bab-Ezzouar, Algiers, Algeria*

Abstract

Structure of ball-milled powder mixtures containing monoclinic zirconia (m-ZrO$_2$) and 15 mol% Y$_2$O$_3$ was analysed. It was shown that the tetragonal Zr$_{0.85}$Y$_{0.15}$O$_{1.93}$ solid solution was formed within 30 min of milling. The structural and magnetic properties were investigated using flame atomic absorption spectrometer, X-ray diffraction, Raman and Mössbauer spectroscopy. The study revealed an increase in fraction of the tetragonal Zr$_{0.85}$Y$_{0.15}$O$_{1.93}$ phase with increasing iron impurity formed due to the wear in the stainless steel assembly. In the course of the ball-milling, the Fe^{3+} concentration increases with milling time promoting the formation of the paramagnetic Zr$_{0.85}$(Y^{3+},Fe^{3+})$_{0.15}$O$_{1.93}$ solid solution. It has been found that there was no sign of tetragonal to metastable m-ZrO$_2$ transition after annealing in the temperature range 500–1100 °C keeping the tetragonal phase rich in Y^{3+} structurally stable. Taking into account the effect of the combined Fe^{3+} and Y^{3+} elements on structural features of the ball-milled product, Fe^{3+} cations promote the mobility of Y^{3+} and consequently diffuse into the tetragonal crystal lattice at room temperature, while Y^{3+} cations act as tetragonal stabilizers at high temperature.

Keywords: Fe-doped yttria-stabilized zirconia, milling, microstructure, Mössbauer spectroscopy

I. Introduction

At room temperature, pure zirconia is monoclinic. As the temperature rises, the monoclinic zirconia (m-ZrO$_2$) changes into tetragonal (t-ZrO$_2$) between 1170 and 2370 °C and finally into a cubic (c-ZrO$_2$) that persists until the melting point [1,2]. Nevertheless, the monoclinic to tetragonal polymorph phase transition causes significant volume change (about 4.7%), which renders the pure material inappropriate for several use cases [3,4]. Stabilizing t-ZrO$_2$ with the addition of aliovalent oversized dopants, notably Ca^{2+}, Mg^{2+} and Y^{3+}, or by adjusting particle size below the critical value of $r_0 \sim 30$ nm, can suppress such disruptive phase transition [5–7]. Depending on the doping concentration, some of the Zr^{4+} cations can be replaced by the oversized aliovalent ions like Y^{3+}. To keep the charge in balance, one oxygen vacancy must be produced for each pair of dopant cations, causing the t-ZrO$_2$ or c-ZrO$_2$ polymorphs to stabilize through the introduction of oxygen vacancies, which reduces the coordination number of Zr^{4+} cations [8–10]. Typically, aliovalent oxides are dissolved into a solid solution to introduce oxygen vacancies within the ZrO$_2$ lattice [8]. This will only happen if the dopant cations have bigger ionic radii than the Zr^{4+} cations, as demonstrated in the work of Raming *et al.* [11]. Nonetheless, by adding the undersized Fe^{2+} and/or Fe^{3+} cations to the ZrO$_2$ lattice, the t-ZrO$_2$ and c-ZrO$_2$ phases should be stabilized at ambient temperature [12]. However, because of their lower ionic radii compared to the Zr^{4+} cations, this stabilization has not proven effective. Moreover, the t-ZrO$_2$→m-ZrO$_2$ phase transition becomes more likely at high temperature [10].

High energy ball milling is one of the preparation techniques that is relatively simple to use in solid-state

*Corresponding author: +213 550857743
e-mail: *a.sari@crnb.dz*

processing allowing Fe^{2+} and/or Fe^{3+} cations to be introduced into to the zirconia lattice in order to exhibit new and unusual properties [13–15]. However, the effect of iron impurity on the polymorphous transformation in zirconia has rarely been reported. Nonetheless, several investigations on yttria-stabilized zirconia with varying Fe concentrations have been conducted to improve structural and mechanical properties, as well as the application range of zirconia ceramics [16]. Stefanic *et al.* [17] found that the presence of contaminants in ball-milled m-ZrO_2 powder affected the stability of the tetragonal zirconia product. Raming *et al.* [18] observed that in completely crystalline tetragonal zirconia, only small amounts of Fe^{3+} (<1 mol%) could dissolve into the zirconia lattice. Shiratori *et al.* [19] investigated how impurities affected the conductivity of composites in the system (1-*x*)3YSZ-*x*MgO. They concluded that the doping of cubic phase 3YSZ with α-Fe_2O_3 led to a decrease in unit cell volume. According to the authors [19], this behaviour resulted from the substitution of the Zr^{4+} cations with the smaller Fe^{3+} cations. Kalam *et al.* [20] discovered that the raising annealing temperatures allows Fe^{3+} cations to segregate out of zirconia and form a α-Fe_2O_3 phase. However, Belous *et al.* [21] found that the solubility of iron in zirconia increases with yttrium content.

In this work we present the investigation of the structural changes and magnetic properties of Fe-doped ZrO_2-15 mol% Y_2O_3 powders mixture produced by high energy ball milling. Considering that the doping of monoclinic zirconia with 15 mol% of Y_2O_3 stabilizes cubic zirconia, as reported in the literature [1], the question arises as to what structural changes are caused by combined doping (Y^{3+} + Fe^{3+}) where iron is systematically incorporated into the powder mixture during the milling in a stainless-steel vessel. However, the question is to know if the monoclinic to tetragonal phase transition observed in course of the first hour of ball-milling is due to the insertion of yttrium oxide into the zirconia or due to the incorporation of iron impurity by the ball-milling medium or whether it is a consequence of reduction in crystallite size introduced by the milling process.

II. Experimental

2.1. Synthesis

The starting powders Y_2O_3 (44 μm, purity 99.99%) and ZrO_2 (44 μm, purity 99.995%) were accurately weighed (using an analytical Sartorius balance), mixed and hand ground for about 30 min under doubly distilled acetone to homogenize the mixture before ball milling. The powders mixture (denoted as ZrO_2-15Y_2O_3) consisted of 0.64 g of Y_2O_3 and 11.36 g of ZrO_2, which corresponded to molar concentration of 85 mol% ZrO_2 and 15 mol% Y_2O_3. After the homogenising the mixture was milled at room temperature using a Fritsch planetary ball mill (Model P5, Fritsch, GmbH, Germany)

equipped with stainless steel balls (20 mm in diameter) and vials (125 ml in volume). The powders mixture was milled in air for 30 min up to 30 h. Seven balls were used and the vials rotated at 500 rpm. Each hour of milling was interspersed with a pause of 30 min to prevent overheating.

2.2. Characterization

During the ball-milling process, the amount of iron and chromium incorporated from the milling media was measured using a flame atomic absorption spectrometer (AAnalyste 400 PerkinElmer, USA). The source of radiation was a Fe hollow cathode lamp running at 248.3 nm and operating at 15 mA.

After ball milling for given times, batches of 300 mg of product were taken out from the vials for crystal structure analysis using an XRD diffractometer (PANalytical X'Pert PRO MPD, Malvern Panalytical Co.). The measurements were carried out under CuKα radiation at 30 kV and 40 mA using a PIXcel 1D detector, with a step size of 0.02° and 2θ range from 15° to 90°. For phase identification, PDF-2 database (ICDD-International Centre for Diffraction Data, Newtown Square, PA) embedded in X'Pert Highscore plus software was used.

The Rietveld analyses method was applied to X-ray diffraction data to obtain accurate structure information for crystalline phases in the ball-milled products. Structural and microstructural parameters were refined by the Rietveld profile analysis method, using the X'Pert High-Score plus software v. 4.9 [22]. Structural parameters described the measurement of phase fraction (%) and unit cell volume ($Å^3$), while microstructural parameters included crystallite size (nm) and lattice strain (%). NIST Silicon SRM 640c certified for line location and line profile for powder diffraction was used as an instrument standard [23] to fit the experimental profiles using a model based on a pseudo-Voigt function [24,25]. Quantitative phase analysis was automatically carried out for each phase throughout the fitting procedure using the HighScore Plus CHUNG method application [26,27].

The un-milled and ball-milled powder mixtures were characterized by Raman spectroscopic technique using an INNOVA 100 spectrometer equipped with a CCD detector refrigerated by liquid nitrogen. Raman spectra were recorded at room temperature in the range 100–1500 cm^{-1} using argon ion laser with the 532 nm excitation line (power ~10 mW).

Mössbauer absorption by Fe was used to measure isomer shift, quadrupole splitting, and hyperfine fields in the selected samples ball-milled for 5 and 30 h containing iron. A Wissel instrument operating with a radioactive ^{57}Fe gamma-quantum source in Rhodium matrix was used with the Recoil software to recorder Mössbauer spectra [28]. Metallic iron was utilized as a reference for isomer shift and energy calibration.

For thermal stability study, the annealing of the

product ball-milled for 30 h was performed *in situ* using high-temperature X-ray diffraction with high-temperature oven chamber HTK1200 (Anton Paar HTK 12, Austria) under air for 2 h at 500, 700, 900 and 1100 °C.

III. Results and discussion

3.1. Structure of milled powders

The estimated values of structural and microstructural parameters were obtained from refined XRD patterns by the Rietveld method [29] using HighScore Plus software. The values of the reduced χ^2 or goodness of fit of all the refined XRD patterns lie within 1.42–1.68. The selected refined XRD patterns corresponding to 0, 0.5, 10 and 30 h of milling are shown in Fig. 1. The structural parameters (phase fraction and unit cell volume) are given in Fig. 2, while the microstructural parameters (crystallite sizes and strain) are presented in Fig. 3. To follow the structural and microstructural changes in the ball-milled products, the total milling time (30 h) was divided in three successive stages: Stage I from 0 to 0.5 h, Stage II from 0.5 to 5 h and Stage III from 5 to 30 h.

Stage I (up to 0.5 h)

The refined X-ray diffraction pattern of the un-milled powder mixture shows the coexistence of individual re-flections of ZrO_2 and Y_2O_3 phases (Fig. 1a). The characteristic peaks were indexed according to the standard: ICDD PDF #01-083-0938 of monoclinic zirconia (m-ZrO_2) and ICDD PDF #01-071-0049 of cubic yttria (c-Y_2O_3). The estimates of their phase fractions were ~75% of m-ZrO_2 and ~25% of c-Y_2O_3 as indicated in Fig. 2a. Obviously, the intensities of their peaks are in accordance with their weight compositions. Moreover, the obtained values of the microstructural parameters indicate that the un-milled m-ZrO_2 phase contains large crystallites of ~50 nm with small strain of ~0.16% (Fig. 3).

After 30 min of milling, new peaks were observed at 2θ 30.03°, 34.95°, 53.51° and 62.58° which matched with the standard ICDD PDF #01-070-4431 identified as $Zr_{0.85}Y_{0.15}O_{1.93}$. The crystal system was tetragonal with crystallite size of ~20 nm, estimated from the refined XRD pattern. In comparison with the un-milled powders mixture, phase fractions of m-ZrO_2 and c-Y_2O_3 dropped suddenly as illustrated in Fig. 2a. It is also found that the phase fraction of tetragonal $Zr_{0.85}Y_{0.15}O_{1.93}$ as well as the strain in m-ZrO_2 increase after 30 min of milling. According to the literature data [30], in the most intensively studied zirconia-yttria (m-ZrO_2-Y_2O_3) system, addition of 15 mol% Y_2O_3 stabilizes the cubic rather than the tetragonal phase which was found in this work. In addition, it has been even found that the addition of more than about 8 mol% Y_2O_3
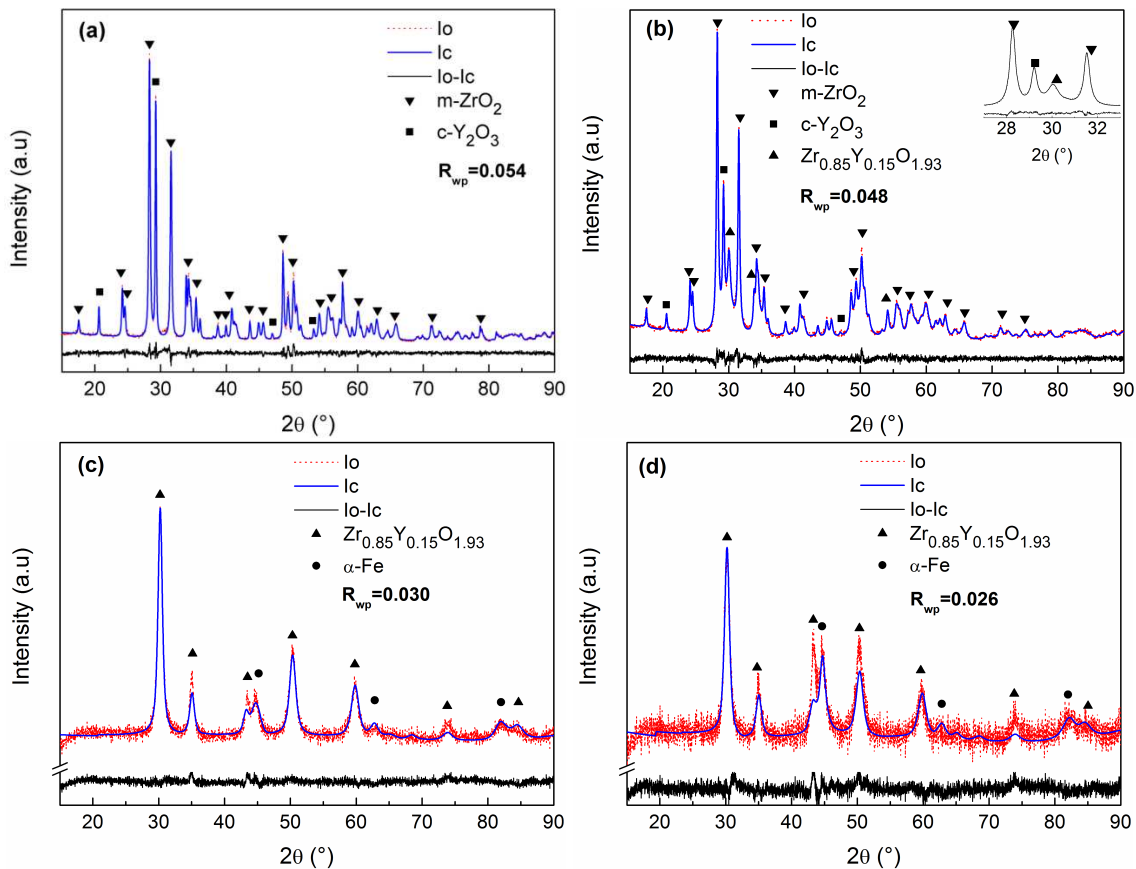

Figure 1. Refined patterns of un-milled and ball-milled products at various times: a) 0 h, b) 0.5 h, c) 10 h and d) 30 h - I_0 **is observed intensity,** I_c **is calculated intensity and** $I_0 - I_c$ **is fitting residual**
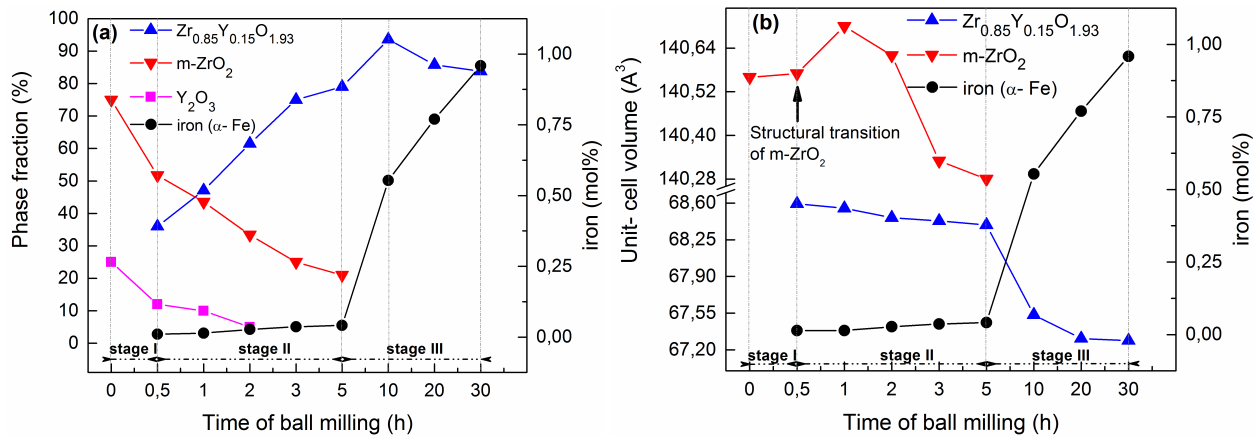
Figure 2. Evolution of phase fractions (a) and unit cell volumes of ZrO_2-15Y_2O_3 powders as a function of milling time
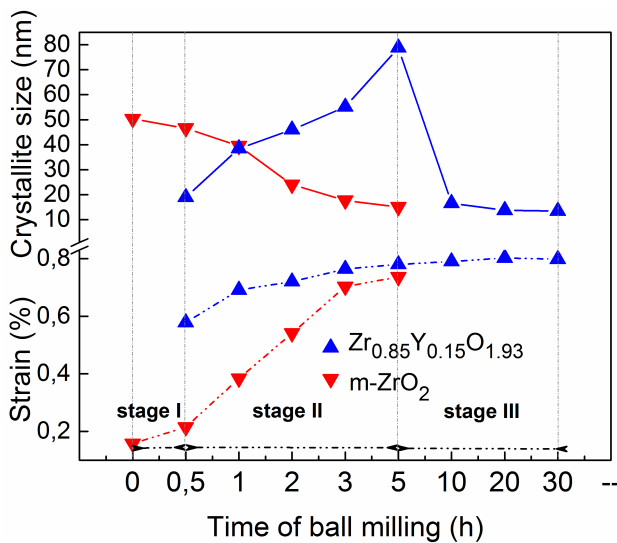

Figure 3. Evolutions of crystallite size and strain of ZrO_2-15Y_2O_3 powders as a function of milling time

stabilizes well the cubic phase (c-ZrO_2) down to room temperature. Nevertheless, Stefanic *et al.* [31] and Zhao *et al.* [32] found that the phase transition from monoclinic (m-ZrO_2) to tetragonal (t-ZrO_2) phase occurred after milling pure monoclinic zirconia powder between 10 and 15 h suggesting that the incorporation of the aliovalent Fe^{3+} into the sample from milling media causes this transition. In addition, Johar *et al.* [33] found that that the amount of cubic phase decreased as the amount of Fe slightly increased in case of ZrO_2-8 mol% Y_2O_3. Accordingly, XRD peaks of iron (α-Fe) are not observed in this stage indicating the dissolution of iron impurity within m-ZrO_2 lattice.

Stage II (from 0.5 to 5 h)

In the milling range 0.5–2 h, m-ZrO_2 fraction decreases from ~52% to ~33% while c-Y_2O_3 fraction reduces to ~5% (Fig. 2a). After further milling up to 5 h, all reflections typical of c-Y_2O_3 disappeared which indicates that yttria is dissolved into the m-ZrO_2 lattice. Knowing that Y^{3+} cations act as monoclinic destabilizers, a decrease in m-ZrO_2 fraction to ~21% was noticed

after 5 h of milling. On the other hand, the concentration of iron impurity slightly increased from 0.01% after 0.5 h of milling to 0.04% for milling time of 5 h (Fig. 2a). In the meantime, phase fraction of m-ZrO_2 continuously decreased and disappeared during milling period 0.5–5 h in the favour of the tetragonal $Zr_{0.85}Y_{0.15}O_{1.93}$ phase formation whose content increased up to ~79% (Fig. 2a).

The unit cell volume of m-ZrO_2 (Fig. 2b) slightly increased with milling time up to 0.5 h leading to the partial phase transition of m-ZrO_2 to tetragonal $Zr_{0.85}Y_{0.15}O_{1.93}$. After 1 h of milling, the unit cell volume of m-ZrO_2 increased to a maximum value estimated to 140.70 Å^3 and then decreased to the minimum value of 140.28 Å^3 after 5 h of milling which was the result of almost complete transition of m-ZrO_2 to $Zr_{0.85}Y_{0.15}O_{1.93}$. Such evolution is due to the smaller ionic radius of Fe^{3+} (0.78 Å) compared to that of Zr^{4+} (0.84 Å) [16] giving rise to a decrease in the unit cell volume of $Zr_{0.85}Y_{0.15}O_{1.93}$. The results given in Figs. 2a and 2b indicate that the iron impurity facilitates the dissolution of yttrium during the formation of a solid solution of the tetragonal phase in which also some iron is dissolved in the zirconia matrix [15]. Similar observations have also been made by Shiratori *et al.* [19] who suggested a decrease of the unit cell volume when the Fe^{3+} cations substituted the Zr^{4+} cations, where the smaller Fe atom had faster diffusion than the larger Y atom having a low activity. Johar *et al.* [33] reported that as the addition of Fe increased, the crystal volume of tetragonal phase tended to decrease because Fe^{3+} cation is smaller than Zr^{4+}. Accordingly, the substitution of Zr^{4+} cations by the undersized Fe^{3+} cations induces the variation in lattice parameter, thus decreases the volume of the unit cell.

Stage III (from 5 to 30 h)

Between 5 and 30 h of milling, the concentration of iron impurity increases fast up to 1 mol% and the unit cell volume of $Zr_{0.85}Y_{0.15}O_{1.93}$ gradually decreases (Figs. 2a and 2b) through the substitution of Zr^{4+} with the undersized Fe^{3+} cations [18]. Also, after milling for 10 h a considerable phase fraction of
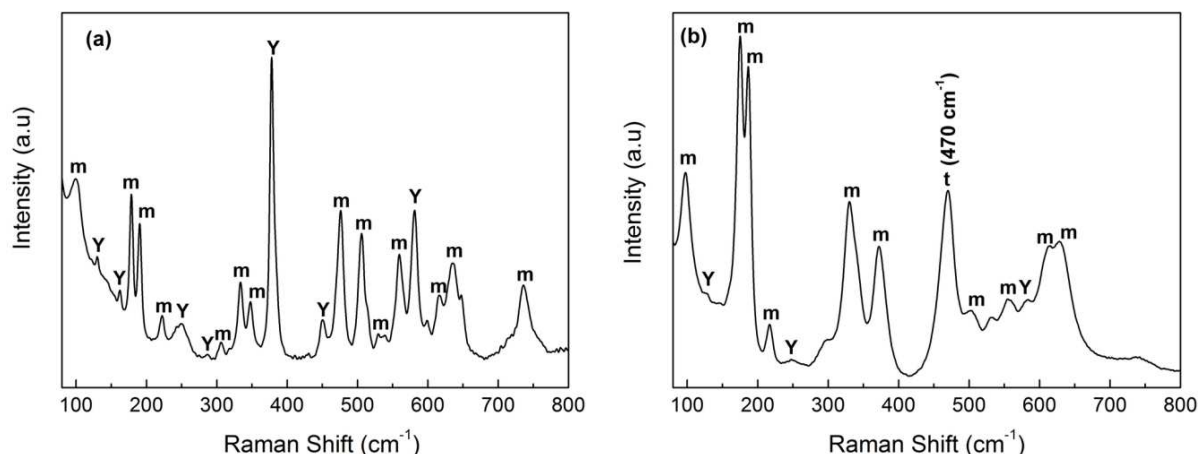
Figure 4. Raman spectra at RT of: a) un-milled and b) powder ball-milled for 0.5 h (m – monoclinic ZrO_2, Y – Y_2O_3, and t – tetragonal $Zr_{0.85}Y_{0.15}O_{1.93}$)

$Zr_{0.85}Y_{0.15}O_{1.93}$ (~94%) was obtained new XRD peaks at $2\theta = 44.7°$, $62.4°$ and $82.2°$ appeared identified as free α-Fe (Fig. 1c). This period of milling characterise complete m-$ZrO_2 \rightarrow$ tetragonal $Zr_{0.85}Y_{0.15}O_{1.93}$ phase transition. Accordingly, the partial phase transition from m-ZrO_2 to $Zr_{0.85}Y_{0.15}O_{1.93}$, observed from the first hour of ball-milling, could be attributed to the stabilizing influence of impurities such as undersized ion Fe^{3+} rather than the effect of crystallite size.

Raman spectroscopy was used to analyse the structural modifications induced by Y_2O_3 and iron impurities. This is based on the fact that different modes attributable to three polymorphs (monoclinic, tetragonal and cubic) were all sufficiently identifiable [34,35]. The Raman spectrum of the un-milled powder mixtures (Fig. 4a) exhibits 14 out of the 18 theoretically predicted bands characteristic of the monoclinic phase at: 100, 179, 190, 222, 306, 334, 348, 382, 475, 506, 536, 560, 616, 637 and 737 cm^{-1} [36–38]. Not all Raman active modes were observed in the un-milled powders mixture, but the spectrum is in good agreement with literature data for monoclinic modification [39]. Additional peaks characteristic of the cubic Y_2O_3 were also found at positions 131, 163, 251, 289, 378, 451 and 581 cm^{-1} [40].

Milling up to 30 min results in the appearance of the most prominent band at 470 cm^{-1} typical of the tetragonal $Zr_{0.85}Y_{0.15}O_{1.93}$ phase (Fig. 4b). This finding is corroborated by the results of X-ray diffraction analyses (Fig. 1b) and results reported by Ghosh *et al.* [41]. However, bands typical of monoclinic phase became weak and broader due to the strongly disordered structure and lowered symmetry arising from the partial substitution of Zr^{4+} by Fe^{3+} cations which give rise to the m-$ZrO_2 \rightarrow Zr_{0.85}Y_{0.15}O_{1.93}$ phase transformation. After 10 h of milling, the nature of the peaks and their position are found to be quite different from that of the un-milled product. Indeed, new bands typical of tetragonal $Zr_{0.85}Y_{0.15}O_{1.93}$ phase were observed at position 144 and 285 cm^{-1} [42]. In addition, the band observed at 470 cm^{-1} disappeared due to the loss of crystallinity induced by ball-milling as already reported in the liter-

ature [43]. However, bands typical for monoclinic ZrO_2 phase disappeared what is in agreement with the XRD results (Fig. 1c).

3.2. Thermal stability of milled powder

For examination of thermal stability, the product ball-milled for 30 h was investigated in situ by X-ray diffraction at 500, 700, 900 and 1100 °C for 2 h (Fig. 5). Moreover, the estimated values for structure and microstructure parameters were obtained by the Rietveld refinement (Table 1). It was found that all the refined XRD patterns of the calcined ball-milled products contain only two phases: $Zr_{0.85}(Y^{3+},Fe^{3+})_{0.15}O_{1.93}$ as the dominant phase and haematite α-Fe_2O_3 (Table 1). Interestingly, the annealing temperature raised in the range 500–1100 °C caused an excretion of the undersized Fe^{3+} cations from the tetragonal lattice and formation of the haematite at the expense of the tetragonal phase (Table 1). Indeed, the results from the Rietveld refinement show that the phase fraction of tetragonal $Zr_{0.85}(Y^{3+},Fe^{3+})_{0.15}O_{1.93}$ decreases slightly from ~61 to ~57%, while the phase fraction of haematite increases slightly from 39 to 43%. On the another hand, the substitution of the Y^{3+} cations thermally activated with the undersized Fe^{3+} cations promotes stability of the tetragonal phase rich in Y^{3+} in the temperature range 500–1100 °C. It is clear from Fig. 5 and Table 1 that the refined XRD patterns appeared to contain only haematite and tetragonal phases. In addition, the crystallite size and unit cell volume of $Zr_{0.85}(Y^{3+},Fe^{3+})_{0.15}O_{1.93}$ phase increased as evidenced by the bigger ionic radii of Y_3^+ cation (1.15 Å) in comparison with those of the Zr^{4+} cation (0.84 Å) [10].

Raman spectrum of the powder mixture ball-milled for 30 h and annealed at 1100 °C for 2 h is shown in Fig. 6. Only two bands characteristic of the tetragonal $Zr_{0.85}Y_{0.15}O_{1.93}$ phase are visible, at 275 cm^{-1} and a broad band at 590 cm^{-1} (Fig. 6). Besides, three additional bands were observed at positions 222, 400 and 1300 cm^{-1} and assigned to the α-Fe_2O_3 [44]. Hence, the phase development in the ball-milled and
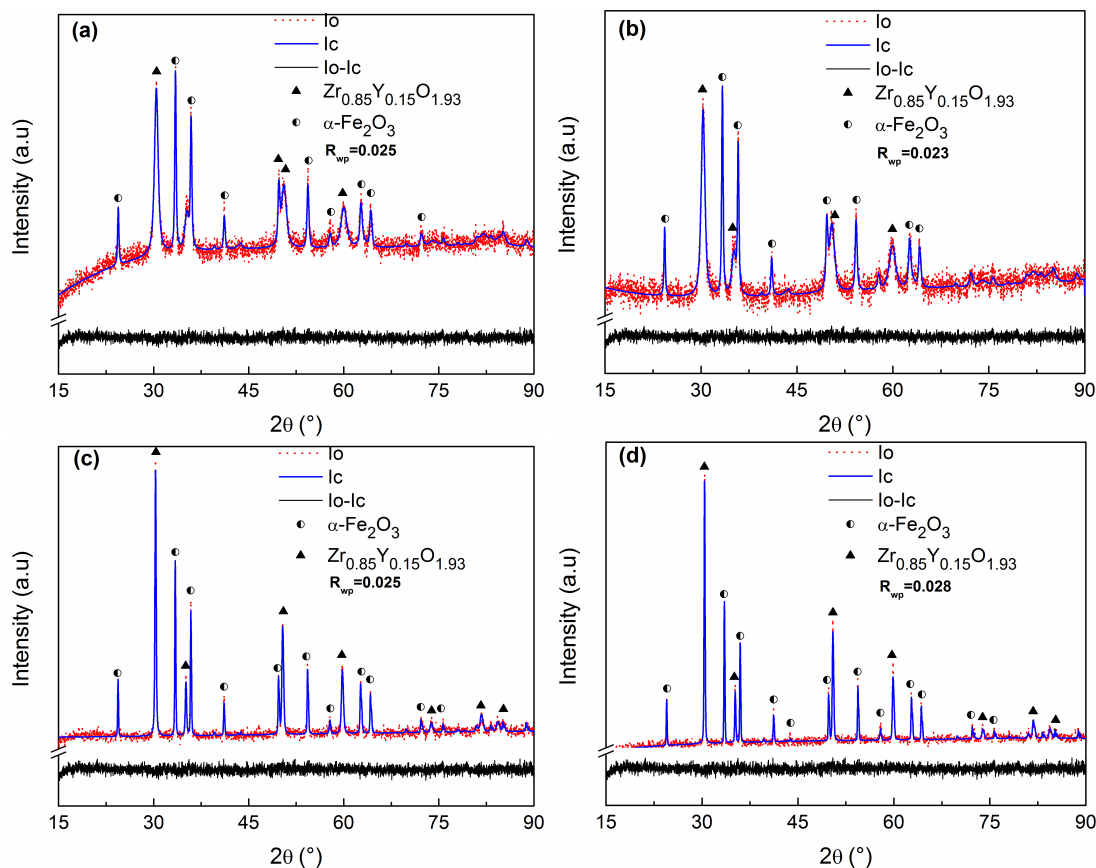
Figure 5. Refined patterns of product ball-milled for 30 h and annealed for 2 h at different temperatures: a) 500 °C, b) 700 °C, c) 900 °C and d) 1100 °C - I_0 **is observed intensity,** I_c **is calculated intensity and** $I_0 - I_c$ **is fitting residual**

Table 1. Structural and microstructural parameters determined from the refinement patterns of ZrO_2-15Y_2O_3 powders mixture ball-milled for 30 h and calcined for 2 h at 500, 700, 900 and 1100 °C

Milling time (temperature)	Phase	Phase fraction [%]	Unit cell volume [Å³]	Crystallite size [nm]	Strains [%]	Reduced χ^2
30 h (500 °C)	T	61	67.42	17.3	0.565	1.16
	H	39	-	54.8	0.126	
30 h (700 °C)	T	60	67.44	18.4	0.623	1.05
	H	40	-	63.2	0.143	
30 h (900 °C)	T	56	67.96	93.3	0.161	1.15
	H	44	-	183.5	0.046	
30 h (1100 °C)	T	57	68.03	252.3	0.094	1.37
	H	43	-	218.4	0.022	

T = tetragonal ($Zr_{0.85}Y_{0.15}O_{1.93}$); H = haematite ($\alpha$- Fe_2O_3)

annealed ZrO_2-15Y_2O_3 powder becomes more apparent and agrees with results of X-ray analysis.

The Mössbauer spectroscopy parameters such as isomer shift, quadrupole splitting and hyperfine fields are useful to provide information on magnetic properties in several oxides containing Fe^{3+} cations introduced from milling media. In this respect, the compiled site properties from site distribution parameters, indicates that the product ball-milled for 5 h contains 54% of the α-Fe component and 46% of the component containing Fe^{3+} cations (Fig. 7a and Table 2). The spectrum of the ball-milled product recorded after 5 h of milling (Fig. 7a) revealed a doublet with an isomeric shift (I.S) equal to 0.383 mm/s and a quadrupole splitting (Q.S)

equal to 0.890 mm/s (Table 2), indicating the presence of the paramagnetic Fe^{3+} component [45]. It was already shown that all the Fe^{3+} cations contributed to the formation of a solid solution of $Zr_{0.85}(Y^{3+},Fe^{3+})_{0.15}O_{1.93}$ after 30 min of milling [18]. In addition, the sextet with a magnetic hyperfine field, $<H_{hf}>$, equal to 33.083 T is characteristic of α-Fe and this value agrees with the reference works [46–49].

The Mössbauer spectrum of the powder ball-milled for 30 h and annealed at 1100 °C is shown in Fig. 7b. A superposition of two doublets, one typical of Fe^{3+} component with I.S of 0.374 mm/s and Q.S value of 0.784 mm/s, and the other typical of haematite (α-Fe_2O_3) with I.S of 0.961 mm/s and Q.S of 2.190 mm/s
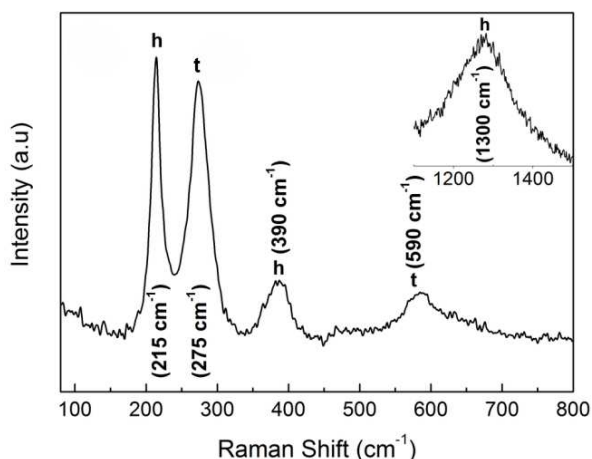
Figure 6. Raman spectra at RT of powders ball-milled for 30 h and annealed at 1100 °C (t – tetragonal $Zr_{0.85}Y_{0.15}O_{1.93}$ and h – haematite)

(Table 2), can be seen. These parameters are consistent with our Raman results and those published for haematite [50–53]. Thus, the prolonged milling and further high-temperature oxidation cause a decrease in the site population of α-Fe component. It was also found that 64% of iron atoms have reacted (Table 2) and were in Fe^{3+} state. The simultaneous presence of Fe^{3+} in tetragonal $Zr_{0.85}(Y^{3+},Fe^{3+})_{0.15}O_{1.93}$ solid solution (27% of Fe^{3+}) and haematite phase (37% of Fe^{3+}) was confirmed (Table 2). This finding agrees with the works of Pashkova [50]. Indeed, during ball-milling process, a

fraction of the Fe^{3+} and Y^{3+} cations were incorporated in the zirconia network while forming the crystalline $Zr_{0.85}(Y^{3+},Fe^{3+})_{0.15}O_{1.93}$ solid solution. Moreover, the insertion of Fe^{3+} cations in the ZrO_2 lattice favours the formation of oxygen vacancies, as shown by the density functional theory (DFT) for Y^{3+} doped ZrO_2 [54,55]. The oxygen vacancies introduced by the oversized aliovalent Y^{3+} contributed to the formation of haematite (α-Fe_2O_3) detected by Mössbauer spectroscopy, which is in good agreement with the previous work of Garcia *et al.* [49].

Combined results of Raman and Mössbauer spectroscopies indicated that the stabilization of $Zr_{0.85}(Y^{3+},Fe^{3+})_{0.15}O_{1.93}$ at room temperature can be attributed to the incorporation of stabilizing aliovalent Fe^{3+} cations into the product due to the wear and oxidation of the milling media. Thus, it is worth noting that even after annealing at 1100 °C, no sign of t-ZrO_2 to m-ZrO_2 phase transition could be detected because the metastable $(Zr^{4+},Fe^{3+})O_2$ phase rich in iron was not formed in contrast to our previous work where this phase was detected using 3 mol% Y_2O_3 [56]. However, as reported by Zhang *et al.* [57] a large amount of surface and interfacial energy is introduced when the crystallite size of m-ZrO_2 was decreased to the nanoscale, hence the free energy of phase transformation was different from the micron-sized structure. Therefore, those unstable phases can exist in the stable or metastable state at room temperature.
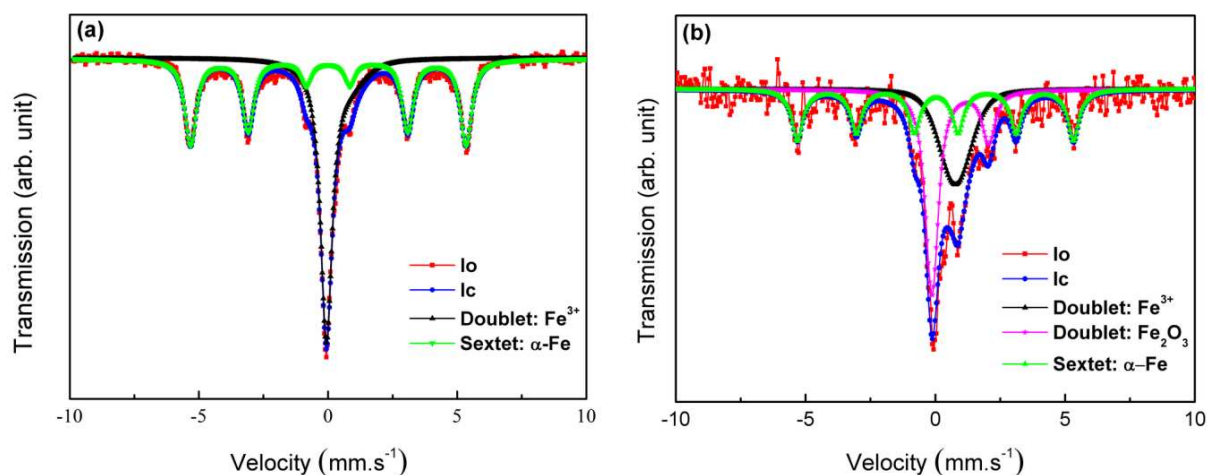

Figure 7. ^{57}Fe Mössbauer spectrum recorded at RT from ZrO_2-15Y_2O_3 powders mixture ball-milled for: a) 5 h and b) 30 h

Table 2. Mössbauer parameters at room temperature of ZrO_2-15Y_2O_3 ball-milled for 5 and 30 h

Milling time	Phase/ions	I.S. [mm/s]	O.S. [mm/s]	H_{hf} [T]	SP [%]
5 h	α-Fe	0.007	0.002	33.083	53.6 (36)
	$(Fe^{3+})_{paramag}$	0.383	0.89	-	46.4 (37)
30 h	α-Fe	0.02	−0.016	32.98	36.0 (73)
	$(Fe^{3+})_{paramag}$	0.374	0.784	-	27.2 (47)
	haematite	0.961	2.190 (22)	-	36.8 (55)

I.S - isomer shift; Q.S - quadrupole splitting; H_{hf} - hyperfine field; SP - site populations of component; $(Fe^{3+})_{paramag}$ - Fe^{3+} in paramagnetic state

IV. Conclusions

Investigation on structural and magnetic properties of the ball-milled Fe-doped ZrO_2-15 mol% Y_2O_3 clearly reveals the following important features:

- Nanocrystalline tetragonal $Zr_{0.85}Y_{0.15}O_{1.93}$ can be mechano-synthesized within 30 min of milling.
- In the early stage of ball-milling, it was noticed that the Fe^{3+} cations, which act as tetragonal phase stabilizers, led to a decrease in unit cell volume of the nanocrystalline $Zr_{0.85}Y_{0.15}O_{1.93}$.
- Raman spectra at room temperature confirm the presence of the tetragonal phase in the ball-milled mixture.
- The Fe^{3+} cations occupied a substitutional site in the paramagnetic $Zr_{0.85}(Y^{3+},Fe^{3+})_{0.15}O_{1.93}$ lattice.
- Phase transition from tetragonal to monoclinic is suppressed in the temperature range 500–1100 °C keeping the tetragonal structure stable.

It was concluded that a partial transition from monoclinic to tetragonal zirconia, observed in earlier ball-milling, should be attributed to the stabilizing influence of Fe^{3+} rather than the effect of decreased crystallite size.

References

1. A. Fernández-Osorio, L. Ramos-Olmos, C.F. Julián, "Black nanocrystalline cubic zirconia: Manganese-stabilized c-ZrO_2 prepared via the solegel method", *Mater. Chem. Phys.*, **147** [3] (2014) 796–803.
2. G. Dell'Agli, C. Ferone, G. Mascolo, M. Pansini, "Crystallization of monoclinic zirconia from metastable phases", *Solid State Ionics*, **127** [3-4] (2000) 223–230.
3. P.M. Steven, I. Brett, S. Amy, "Cation coordination and interstitial oxygen occupancy in co-doped zirconia from first principles", *Solid State Ionics*, **227** (2012) 66–72.
4. K. Gurushantha, K.S. Anantharaju, H. Nagabhushana, "Facile green fabrication of iron-doped cubic ZrO_2 nanoparticles by Phyllanthus acidus: Structural, photocatalytic and photoluminescent properties", *Mater. Proceed.*, **397** (2015) 36–47.
5. A. Navrotsky, "Thermochemical insights into refractory ceramic materials based on oxides with large tetravalent cations", *J. Mater. Chem.*, **15** [19] (2005) 1883–1890.
6. S.A. Ostanin, E.I. Salamatov, "Microscopic mechanism of stability in yttria-doped zirconia", *JETP Letters*, **74** [11] (2001) 625–629.
7. T. Chraska, A. H. King, C. Berndt, "On the size-dependent phase transformation in nanoparticulate zirconia", *Mater. Sci. Eng.*, **286** [1] (2000) 169–178.
8. L. Song, Q. Zhang, J. Ma1, C. Chen, B. Xu, M. Zhu, X. Xu, N. Cewen, Z. Shen, "Vacancy-ordered yttria stabilized zirconia as a low-temperature electronic conductor achieved by laser melting", *J. Eur. Ceram. Soc.*, **39** [4] (2018) 1374–1380.
9. J.R. Kelly, I. Denry, "Stabilized zirconia as a structural ceramic: An overview", *Dental Mater.*, **24** [3] (2008) 289–298.
10. S. Fabris, A. T. Paxton, M.W. Finnis, "A stabilization mechanism of zirconia based on oxygen vacancies only", *Acta Mater.*, **50** [20] (2002) 5171–5178.
11. D.I. Raming, V.A. Gritsenko, T.V. Perevalov, "Oxygen vacancies in zirconium oxide as the blue luminescence centres and traps responsible for charge transport: Part I – Cristals", *Crys. Mater.*, **15** (2021) 100979.
12. C.J. Howard. R.J. Hill, B.E. Reichert, "Structures of the ZrO_2 polymorphs at room temperature by high-resolution neutron powder diffraction", *Acta Cryst.*, **B44** (1988) 116–120.
13. L. Ferris, M. Allwes, L. Diamandescu, A. Perrin, M. McHenry, M. Sorescu, "Fundamental studies of hafnia-hematite nanoparticles", *J. Phys. Chem. Sol.*, **145** (2020) 109567.
14. N. Doufar, M. Benamira, H. Lahmar, M. Trari, I. Avramova, M.T. Caldes, "Structural and photochemical properties of Fe-doped ZrO_2 and their application as photocatalysts with TiO_2 for chromate reduction", *J. Photochem. Photobio.*, **386** (2020) 112105.
15. I.Yu. Prokhorov, G.Ya. Akimov, V.M. Timchenko, "Stability of structural materials based on ZrO_2", *Refract. Ind. Ceram.*, **39** (1998) 189–197.
16. H. Nakajima, K. Itoh, H. Kaneko, Y. Tamaura, "Effects of Fe doping on crystalline and optical properties of yttria-stabilized zirconia", *J. Phys. Chem. Sol.*, **68** [10] (2007) 1946–1950.
17. G. Stefanic, S. Music, A. Gajovic, "A comparative study of the influence of milling media on the structural and microstructural changes in monoclinic ZrO_2", *J. Eur. Ceram. Soc.*, **27** [2-3] (2007) 1001–1016.
18. T.P. Raming, A.J.A. Winnubst, W.E. Van Zyl, H. Verweij, "Densification of zirconia-hematite nanopowders", *J. Eur. Ceram. Soc.*, **23** [7] (2003) 1053–1060.
19. Y. Shiratori, F. Tietz, H.J. Penkalla, J.Q. He, Y. Shiratori, D. Stover, "Influence of impurities on the conductivity of composites in the system $(3YSZ)_{1-x}$-$(MgO)_x$", *J. Power Sources*, **148** [15] (2005) 32–42.
20. K. Kalam, H. Seemen, P. Ritslaid, M. Rähn, A. Tamm, K. Kukli, A. Kasikov, J. Link, R. Stern, S. Dueñas, H. Castán, H. García, "Atomic layer deposition and properties of ZrO_2/Fe_2O_3 thin films", *Beilstein J. Nanotechnol.*, **9** (2018) 119–128.
21. A.G. Belous, E.V. Pashkova, O.I. Vyunov, "Effect of combined doping (Y^{3+} + Fe^{3+}) on structural features of nanodispersed zirconium oxide", *J. Mater. Sci.*, **40** (2005) 5273–5280.
22. T. Degen, M. Sadki, E. Bron, U. König, G. Nenert, "The HighScore suite", *Powder Diffraction*, **29** [S2] (2014) S13–S18.
23. National Institute of Standards and Technology, "Silicon SRM 640c certified for Line Position and Line Shape Standard for Powder Diffraction", *Certificate of Standard Reference Material 640c*, 2000.
24. R. Kumar, E. Jordan, M. Gell, J. Roth, C. Jiang, J. Wang, S. Rommel, "CMAS behavior of yttrium aluminum garnet (YAG) and yttria-stabilized zirconia (YSZ) thermal barrier coatings", *Surf. Coat. Technol.*, **327** [25] (2017) 126–138.
25. P. Scardi, M. Leoni, "Line profile analysis: Pattern modelling versus profile fitting", *J. Appl. Cryst.*, **39** (2006) 24–31.
26. F.H. Chung, "Quantitative interpretation of X-ray diffraction patterns of mixtures. I. Matrix-flushing method for quantitative multicomponent analysis", *J. Appl. Crys.*, **7** (1974) 519–525.
27. S. Jung, "Quantitative analysis of Fe-Mo alloys by X-ray

fluorescence spectrometry", *Am. J. Anal. Chem.*, **5** [12] (2014) 766–774.

28. K. Lagarek, D. Rancourt, S.K. Bose, B. Sanyal, R.A. Dunlap, "Observation of a composition-controlled high-moment/low moment transition in the face centered cubic Fe-Ni system: Invar effect is an expansion, not a contraction", *J. Magn. Magn. Mater.*, **236** [1-2] (2001) 107–130.

29. P. Scardi, L. Lutterotti, A. Tomasi, "XRD characterization of multilayered systems", *Thin Solid Films*, **236** [1-2] (1993) 130–134.

30. A. Tikhonovsky, M. Bartsch, U. Messerschmidt, "Plastic deformation of yttria stabilized cubic zirconia single crystals I. Activation parameters of deformation", *Phys. Stat. Sol.*, **201** [1] (2004) 26–45.

31. G. Stefanic, S. Music, A. Gajovic, "Structural and microstructural changes in monoclinic ZrO_2 during the ball-milling with stainless steel assembly", *Mater. Res. Bull.*, **41** [4] (2006) 764–777.

32. H. Zhao, X. Li, F. Ju, U. Pal, "Effects of particle size of 8 mol% Y_2O_3 stabilized ZrO_2 (YSZ) and additive Ta_2O_5 on the phase composition and the microstructure of sintered YSZ electrolyte", *J. Mater. Proc.*, **200** [1-3] (2008) 199–204.

33. B. Johar, N.A. Zaili, "Fe-doped 8YSZ at different composition for solid electrolyte in solid oxide fuel cell", *2nd International Conference on Green Design and Manufacture 2016, MATEC Web of Conferences*, **78** (2016) 01102.

34. L. Meijun, F. Zhaochi, X. Guang, Y. Pinliang, X. Qin, L. Can, "Phase transformation in the surface region of zirconia detected by UV Raman spectroscopy", *J. Phys. Chem. B*, **105** [34] (2001) 8107–8111.

35. T. Hirata, E. Asari, M. Kitajima, "Infrared and Raman spectroscopic studies of ZrO_2 polymorphs doped with Y_2O_3 and CeO_2", *J. Solid State Chem.*, **110** [2] (1994) 201.

36. D.W. Lui, C.H. Perry, W. Wang, R.P. Ingel, "Low frequency Raman spectra in disordered cubic zirconia at elevated temperatures", *J. Appl. Phys.*, **62** (1987) 250–253.

37. M. Ishigame, E. Yoshida, "Study of the defect-induced Raman spectra in cubic zirconia", *Solid State Ionics*, **23** [3] (1987) 211–218.

38. A. Feinberg, C.H. Perry, "Structural disorder and phase transitions in ZrO_2-Y_2O_3 system", *J. Phys. Chem. Solids*, **42** [6] (1981) 513–518.

39. S.N. Basahel, Tarek T. Ali, K. Narasimharao, A.A. Bagabas, M. Mokhtar, "Effect of iron oxide loading on the phase transformation and physicochemical properties of nanosized mesoporous ZrO_2", *Mater. Res. Bull.*, **47** [11] (2012) 3463–3472.

40. Y. Masatomo, L. Jin-Ho, K. Masato, Y. Masahiro, "Infrared photoluminescence and Raman spectra in the Y_2O_3–ZrO_2 system", *J. Phys. Chem. Solids*, **58** [10] (1997) 1593–1597.

41. A. Ghosh, A.K. Suri, M. Pandey, S. Thomas, "Nanocrystalline zirconia-yttria system a Raman study", *Mater. Let.*, **60** [9-10] (2006) 1170–1173.

42. J.F. Wang, R. Ren, Z.C. Huang, R. Zhou, W. Pan, "Structure characterization calculation of tetragonal zirconia",

Mater. Sci. Eng., **18** [20] (2011) 202008.

43. M. Veithen, Ph. Ghosez, "First-principles study of the dielectric and dynamical properties of lithium niobate", *Phys. Rev. B*, **65** (2002) 214302.

44. T. Tokubuchi, R. Imran, P. Zhenhua, K. Katayamaa, A. Turak, W.Y. Sohn, "Enhanced photo electrochemical water splitting effiency of hematite (α-Fe_2O_3)-based photo electrode by the introduction of maghemite (γ-Fe_2O_3) nanoparticles", *J. Photochem. Photobio.*, **410** (2021) 113179.

45. A.G. Belous, E.V. Pashkova, A.N. Makarenko, V.P. Ivanitskii, O.I. V'yunov, A.V. Ragulya, "Mössbauer study of tetragonal ZrO_2-Y_2O_3-Fe_2O_3 solid solutions", *Inorg. Mater.*, **40** [11] (2004) 1196–1203.

46. F.L. Garcia, V.G. de Resende, E.A. Peigney, A. Barnabe, C. Laurent, "Iron-stabilized nanocrystalline ZrO_2 solid solutions: Synthesis by combustion and thermal stability", *Mater. Res. Bull.*, **44** [6] (2009) 1301–1311.

47. F.J. Berry, M.H. Loretto, M.R. Smith, "Iron-zirconium oxides: An investigation of structural transformations by X-ray diffraction, electron diffraction, and iron-57 Mössbauer spectroscopy", *J. Solid State Chem.*, **83** [1] (1989) 91–99.

48. C. Janot, "Effet Mössbauer et Applications à la Physique du Solide", *Pure Appl. Chem.*, **48** [1] (1976) 53–64.

49. F. Garcia, N. Le Bolay, C. Frances, "Changes of surface and volume properties of calcite during a batch wet grinding process", *Chem. Eng. J.*, **85** [2-3] (2002) 177–187.

50. E.V. Pashkova, A.G. Belous, O.I. V'yunov, V.P. Ivanitskii, "Effect of iron oxide on structure of Y-stabilized zirconia ceramic", pp. 279–285 in *Fuel Cell Technologies: State and Perspectives*, NATO science Series Vol. **202**, Springer, 2005.

51. O.C. Kistner, A.W. Sunyar, "Evidence for quadrupole interaction of Fe^{57m}, and influence of chemical binding on nuclear gamma-ray energy", *Phys. Rev. Lett.*, **4** [8] (1960) 412–415.

52. G. Shirane, D.E. Cox, S.L. Ruby, "Mossbauer study of isomer shift, quadrupole interaction, and hyperfine field in several oxides containing Fe^{57}", *Phys. Rev.*, **125** [4] (1962) 1158–1165.

53. S.A. Kirillova, O.V. Almjasheva, V.V. Panchuk, V.G. Semenov, "Solid-phase interaction in ZrO_2-Fe_2O_3 nanocrystalline system", *Phys. Chem. Math.*, **9** [6] (2018) 763–769.

54. D. Sangalli, A. Debernardi, "Exchange-correlation effects in the monoclinic to tetragonal phase stabilization of yttrium-doped ZrO_2: A first-principles approach", *Phys. Rev. B*, **84** (2011) 214113.

55. R. Terki, G. Bertranda, H. Aourag, C. Coddet, "Structural and electronic properties of zirconia phases: A FP-LAPW investigations", *Mater. Sci. Semicond. Process.*, **9** [6] (2006) 1006–1013.

56. A. Sari, M. Keddam, A. Guittoum, "Effect of iron impurity on structural development in ball-milled ZrO_2-3 mol% Y_2O_3", *Ceram Int.*, **41** [1] (2015) 1121–1128.

57. P. Zhang, K.L. Choy, "The synthesis of single tetragonal phase zirconia by sol-gel route", *Int. J. Eng. Res. Sci.*, **1** [7] 2015 18–24.